Acta Materialia 289 (2025) 120917

Contents lists available at ScienceDirect

Acta Materialia

journal homepage: www.elsevier.com/locate/actamat

Full length article

# How peritectic melting forms bicontinuous microstructures

Zhongyang Li [a], Lukas Lührs [a], Tobias Krekeler [b], Jörg Weissmüller [a,c,*]

[a] Institute of Materials Physics and Technology, Hamburg University of Technology, Hamburg, Germany
[b] Electron Microscopy Unit, Hamburg University of Technology, Hamburg, Germany
[c] Institute of Hydrogen Technology, Helmholtz-Zentrum Hereon, Geesthacht, Germany

ARTICLE INFO

*Keywords:*
Liquid film migration
TiAg alloy
Bicontinuous structure
Dealloying
Peritectic melting

ABSTRACT

Fine-scale porous or bicontinuous microstructures may be prepared by liquid-metal dealloying (LMD). Reverse peritectic reactions, and specifically the peritectic melting of TiAg, have been proposed as dealloying-like processes that produce quite similar microstructures but avoid the restrictions on sample size inherent in LMD. Here, studies of the microstructure evolution during peritectic melting of TiAg suggest a formation mechanism that is not LMD-like but rather relies on the migration of liquid films. The process starts with wetting of the TiAg grain boundaries by the alloy melt. Successively, both Ti and Ag continue to dissolve from one side of the wetted boundary, while $\beta$-Ti deposits on the opposite side and the liquid film sweeps the pristine TiAg crystal. TiAg-Ti interfaces with well-defined orientation relationship and with concentration gradients support this picture, as does the phase morphology in partially decomposed samples. The process generates a bicontinuous structure with a solid Ti skeleton, interpenetrated by the Ag-rich melt. The bicontinuity is conserved even after coarsening. Upon quenching, the Ti phase transforms to $\alpha$-Ti. This study clarifies the mechanism of peritectic melting in TiAg, and it may provide a basis for identifying other alloy systems suitable for producing bicontinuous microstructures by that process.

## 1. Introduction

Dealloying is an important technique for producing porous metals [1–4]. In chemical or electrochemical dealloying, the less noble component dissolves driven by spontaneous or electrochemically induced reactions [5–7]. More recent dealloying methods include liquid metal dealloying (LMD) [8] and vapor-phase dealloying [9]. During the LMD process, the sacrificial component dissolves into the liquid metal, which has a negative enthalpy of mixing with the dissolving component [10]. In vapor-phase dealloying, one component selectively evaporates due to its high vapor pressure [11]. In each case, the formation of a nano- or microscale (network) product structure involves an instability of the dissolution interface — typically the bifurcation of pore channels — and a reorganization of the non-dissolved component by lateral diffusion along the interface [10,12].

Despite differences in kinetic behavior, the aforementioned dealloying processes all require mass exchange with the environment. In other words, the dissolved component is transported out of the product structure by diffusion at the scale of the sample size. This imposes restrictions on the maximum sample size.

The recent discovery of peritectic melting as a new method for internal dealloying [13] provides an exception. As the intermetallic compound TiAg experiences a reverse peritectic reaction upon heating, it converts to solid Ti and liquid Ag as two contiguous phases. The bicontinuous character of the microstructure is conserved after quenching. Furthermore, either porous Ti or porous Ag can be obtained by chemically removing the other component. As the reverse peritectic reaction requires no mass exchange with the environment, large sample sizes may become accessible. Here, we ask in how far the microstructure evolution during peritectic melting rests on the same mechanisms as dealloying.

Ref. [13] tentatively proposes that a dealloying-like mechanism acts during peritectic melting of TiAg, while suggesting that further studies are needed. In that context it may appear significant that bicontinuous microstructures, as well as their porous complements emerging when one phase is selectively etched out, were recently found in Cu–In after partial melting [15]. That scenario is similar to peritectic melting by also avoiding mass exchange with the environment. Yet, the microstructure here evolves not by dealloying but rather by the migration of liquid films wetting grain boundaries in a two-phase alloy, between solidus and liquidus of the alloy phase diagram. The mechanism is distinct from dealloying, as the diffusive transport is here dominantly normal to the interface. Given the similarity between partial and peritectic melting (both involve the decomposition of a solid phase into a solid phase

* Corresponding author at: Institute of Materials Physics and Technology, Hamburg University of Technology, Hamburg, Germany.
*E-mail address:* weissmueller@tuhh.de (J. Weissmüller).

https://doi.org/10.1016/j.actamat.2025.120917
Received 10 December 2024; Received in revised form 13 February 2025; Accepted 7 March 2025
Available online 15 March 2025

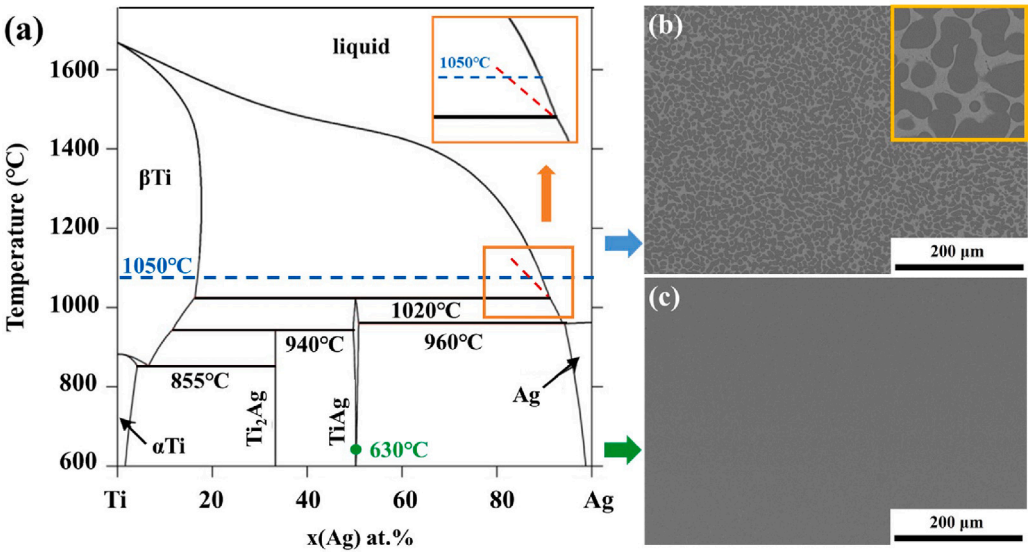


**Fig. 1.** Phase structure before and after peritectic melting. (a) Ti–Ag phase diagram (after [14]), the blue dashed line shows the annealing temperature while the green dot shows the homogenization temperature. Red dashed line is extrapolated from the liquidus line below peritectic line, representing the constrained-equilibrium liquidus line with TiAg phase. (b) Backscattered electron (BSE) image of sample after annealing at 1050 °C for 4 min. Two phases can be clearly observed. A zoomed in image of the microstructure is inserted at the top right corner. (c) BSE image of sample after homogenization at 630 °C 7 days, only one single phase can be found. These structure agree well with the prediction from the phase diagram. (For interpretation of the references to colour in this figure legend, the reader is referred to the web version of this article.)

and a liquid phase), one may speculate if the bicontinuous structure observed after peritectic melting of TiAg also results from liquid film migration (LFM). Indeed, the present study supports that notion.

LFM is established as a transport pathway for compositional equilibration, typically after temperature change [16,17]. During LFM, atoms from a parent grain dissolve into the liquid film and reprecipitate on the opposite side of the grain boundary, with a composition that is closer to equilibrium [16]. LFM is distinguished from diffusion-induced grain boundary migration and from discontinuous precipitation by the presence of the liquid [18,19]. LFM has been observed in various processes including sintering [17,20,21], brazing [22–24], welding [25,26], and peritectic solidification [27,28]. A standard LFM scenario is partial melting, where solid and liquid coexist in equilibrium between solidus and liquidus. Observations include Al–Cu [17], Co–Cu [29], Mo–Ni [16], Cu–In [30], Fe–Al–Zn [31], and also ceramic systems, for example, $ZrO_2$–$Y_2O_3$ [32], $ZrO_2$–$CeO_2$ [33], TiC–Fe [34], and TiN–Ni–TiC [35].

While studies of peritectic melting have been scarce, phase field simulation [36,37] has predicted LFM as a possible mechanism during that process, and have linked that mechanism to dendrite fragmentation in Ti–Al [38]. However, direct experimental evidence for LFM during peritectic melting has yet to be observed.

Investigating peritectic melting of TiAg, we here unravel how the microstructure evolves by LFM and we emphasize the distinction to dealloying.

## 2. Experimental details

TiAg intermetallic compound samples were prepared by induction melting under Ar, based on Ti (> 99.99%) pellets and Ag (> 99.99%). The ingots were vacuum-sealed in quartz, homogenized for 7 days at 630 °C and then cut into small cuboids with the size of $1\times1\times2\ mm^3$. For peritectic melting, the samples were inserted in a 1050 °C pre-heated tube furnace in air for various time, then immediately quenched in room-temperature water.

Some samples where etched to obtain microporous metal. For porous Ti, the Ag was removed with 4 M $HNO_3$; for porous Ag, the Ti was dissolved by concentrated HCl. Both protocols used free corrosion at room temperature for 5 days.

Microstructure observation was conducted on both massive and porous samples. Massive samples were initially ground with abrasive paper, starting from 320 grit and progressing to 4000 grit, followed by polishing with colloidal silica suspension. These samples were then examined under scanning electron microscopy (SEM, Zeiss Supra VP55). Porous samples were cleaned with ethanol and cleaved with a scalpel to expose the fracture surface. Some partially decomposed samples were etched and then vacuum embedded at 60 °C with epoxy. Then these samples were prepared in the same manner as the massive SEM samples. Phase identification was based on Bragg–Brentano X-ray diffraction with Ni-filtered Cu $K_\alpha$ radiation, examining cross-sectional surfaces that were ground with abrasive paper to 2500 grit.

The 100 nm thick transmission electron microscopy (TEM) sample was prepared by gallium focused ion beam (FIB) cutting in a Thermo Scientific Helios Nanolab G3 UC and investigated in a Thermo Scientific Talos F200X, including energy-dispersive X-ray (EDX) analysis.

## 3. Results

### 3.1. Microstructure after peritectic melting

Fig. 1(a) shows the Ti–Ag alloy phase diagram, illustrating that a single-phase state, the intermetallic compound TiAg, is expected for our homogenized samples. Above the peritectic temperature, 1020 °C, TiAg decomposes into the $\beta$-Ti-based solid solution and the Ag-rich melt. For simplicity, in this study, these two solution phases will be denoted as $\beta$-Ti and Ag respectively. The single-phase state after homogenization is confirmed by the SEM image of Fig. 1(c) and by the X-ray diffractogramm, black line in Fig. 2, in which all Bragg reflections can be labeled as TiAg (JCPDS file number 06-0560 [41], Ref. [39]).

In our studies, the reverse peritectic transition was initiated by annealing for various periods of time, with the temperature in each case at 1050 °C, and this was followed by quenching. After annealing for 2 min, the diffractogram (red line in Fig. 2) shows a superposition of TiAg, Ag (JCPDS file number 04-0783 [41], Ref. [42]) and $\alpha$-Ti (JCPDS file number 44-1294 [41], Ref. [43]) reflections, suggesting that the sample has partially decomposed. Diffraction reference patterns in Fig. 2 indicate Bragg reflection positions, $2\theta$, of all phases, and symbols mark the dominant phase contribution to each experimental reflection. Note that the Ag (111) reflection at $2\theta = 38.1°$ can hide a weak

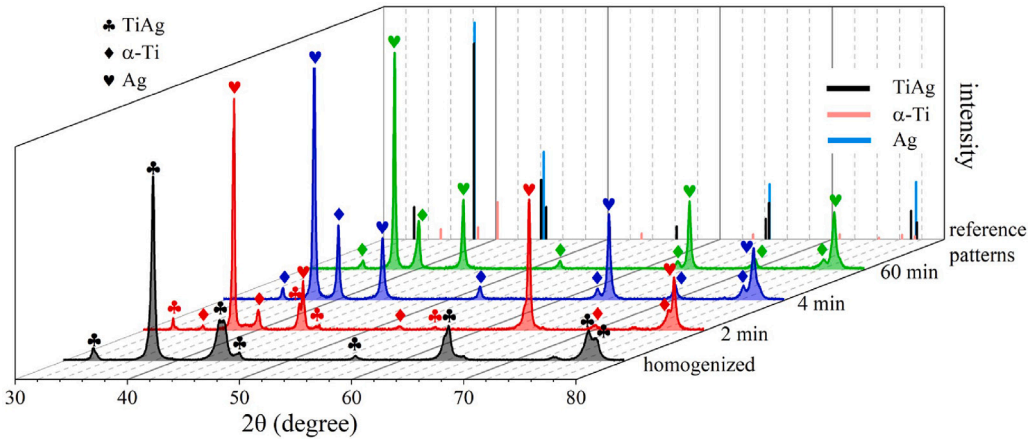


**Fig. 2.** X-ray diffraction on samples after homogenization and after annealing at 1050 °C for 2, 4 or 60 min and quenching. Only TiAg phase can be detected in the as-homogenized sample (gray). Diffraction peaks for both $\alpha$-Ti and TiAg can be seen from 2 min sample (red), suggesting an incomplete decomposition. Disappearance of the TiAg peaks in 4 min and 60 min samples (blue and green, respectively) indicates complete decomposition of TiAg. Symbols link Bragg reflections to phases, see legend. Vertical lines show Bragg reflection positions in reference patterns. (For interpretation of the references to colour in this figure legend, the reader is referred to the web version of this article.)

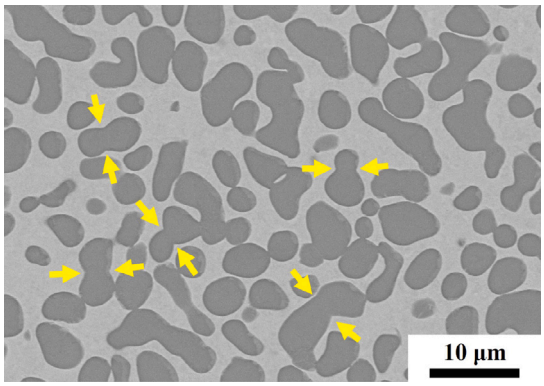


**Fig. 3.** Backscattered electron image of sample after annealing at 1050 °C for 60 min. Yellow arrows mark the position of incompletely wetted grain boundaries.

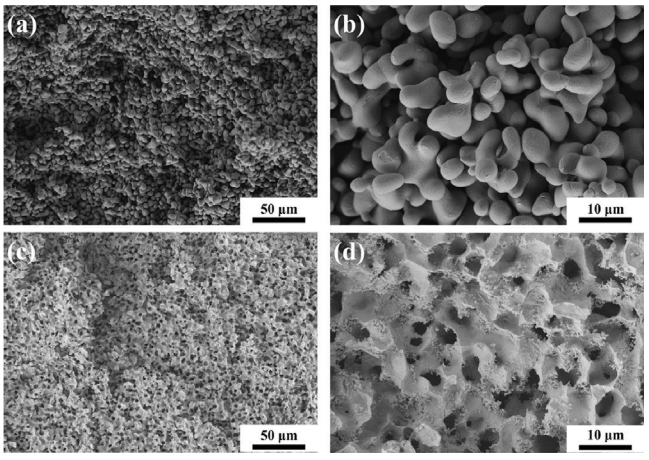


**Fig. 4.** Secondary electron images of (a, b) porous Ti and (c, d) porous Ag. After annealing for 4 min and subsequent quenching, corrosion in different assets served to remove selectively Ti or Ag. Porous Ti shows a ligament-like structure, while the porous Ag has an inverted dealloying structure. These two physically continuous phases confirm the bicontinuous structure obtained after peritectic melting and quenching.

contribution from $\alpha$-Ti (002) at 38.4°; the $\alpha$-Ti phase fraction is manifest in the $\alpha$-Ti (101) reflection at 40.2°.

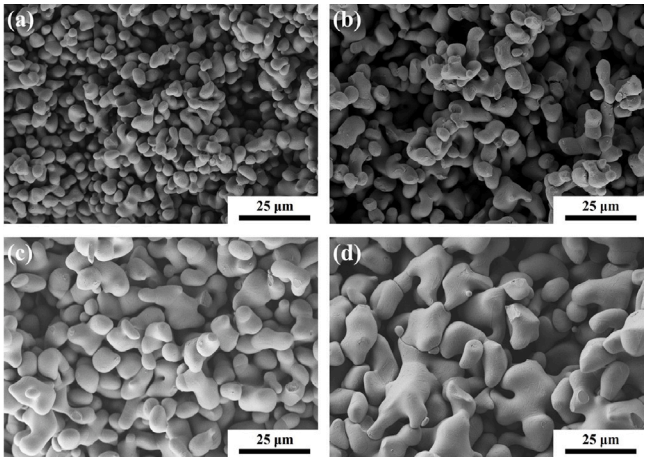


**Fig. 5.** Secondary electron images of porous Ti. The samples went through annealing at 1050 °C for (a) 4 min; (b) 10 min; (c) 20 min; (d) 60 min. Ag phase was removed by chemical etching in 4 M $HNO_3$. The robust sample after corrosion suggests great connectivity of Ti network during annealing.

The SEM micrograph of Fig. 1(b) shows the microstructure after 4 min of annealing as a uniform distribution of two phases. Higher atomic number brings brighter contrast in backscattered electron (BSE) mode; together with the diffractogramm (blue line in Fig. 2) this suggests that the darker and lighter regions in the SEM images represent $\alpha$-Ti solid solution (here referred to as $\alpha$-Ti) and Ag, respectively. This suggests that the reverse peritectic reaction is here complete.

The phases after annealing and quenching are consistent with the alloy phase diagram, which shows TiAg to decompose into $\beta$-Ti and liquid Ag. The quenching is fast enough to suppress the peritectic reaction, yet $\beta$-Ti will transform to $\alpha$-Ti, as indicated by the diffraction results.

After annealing for 60 min, the diffraction result (Fig. 2, green line) remains practically identical to the 4 min one. The SEM micrograph of that state, Fig. 3, shows most of the Ti grain surfaces wetted by the Ag melt. Grain orientation is not communicated by the micrograph and attempts at electron backscatter diffraction imaging failed. Yet, Ti regions in the micrograph regularly show constrictions that must be identified with Ti–Ti–Ag triple lines. This shows that Ti grain boundaries are only partially wet by the Ag melt at the annealing temperature.

Porous samples were prepared by etching out either the Ti or the Ag phase from the 4-min annealed material. As illustrated in Figs. 4(a)

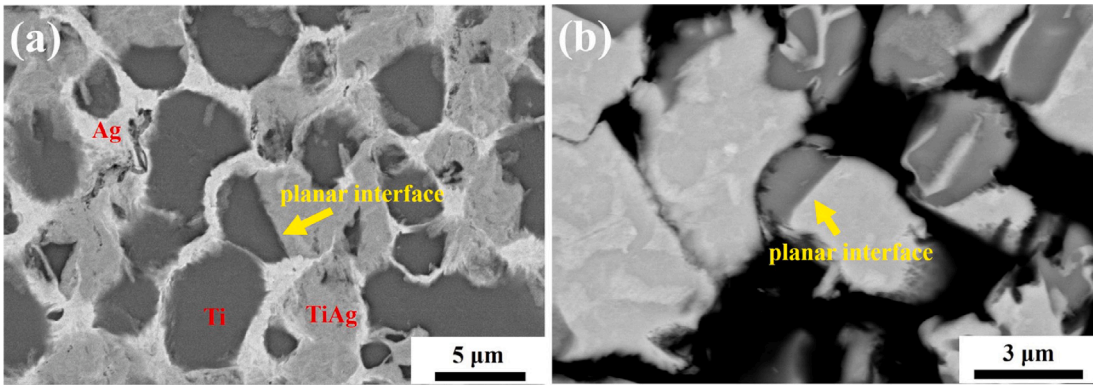


**Fig. 6.** Microstructure of partially decomposed TiAg. (a) Backscattered electron (BSE) image of the cross section, three phases including Ti, Ag and TiAg can be observed. The newly formed Ti phase is attached to the TiAg phase. (b) BSE image of sample after etching and vacuum embedding, Ag phase is replaced by epoxy. Planar interfaces between Ti and TiAg can be seen in both images. Weak contrast in TiAg phase is an artifact from polishing; brighter contrast lines in Ti regions represent undissolved TiAg.

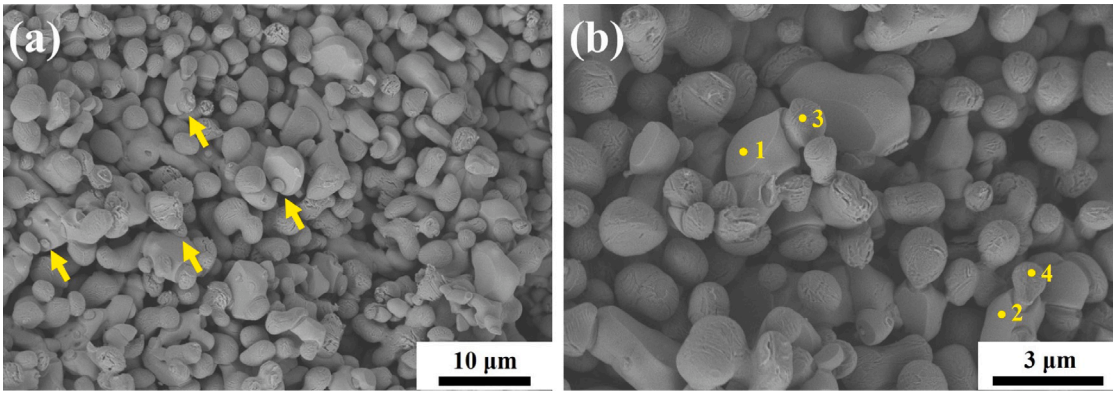


**Fig. 7.** Secondary electron images showing the cleavage surface of a partially decomposed sample from which the Ag phase has been etched out. Two phases with distinct structure can be observed, which is identified as TiAg (with planar and smooth surfaces, see point 1, 2) and Ti (with rough surfaces, see point 3, 4) phase from energy-dispersive X-ray result.

and (b), removing the Ag reveals Ti to form a network-like ligament structure. Conversely, removing the Ti reveals Ag with an inverted dealloying structure (Figs. 4 (c, d)). A similar structure has been documented in other LMD metals [44]. Both bulk samples remained stable after the removal of Ti or Ag phase, suggesting that each phase is contiguous. This confirms that peritectic melting of TiAg produces a bi-continuous structure [13].

Porous samples were also prepared from alloy states after longer anneals, so as to investigate the microstructure evolution at the annealing temperature. As can be seen from Fig. 5, the ligament size of the Ti phase increased from about 4 μm (after 4 min of annealing, see Fig. 5(a)) to around 10 μm (after 60 min of annealing, see Fig. 5(d)). The complete removal of the Ag phase and the robust Ti network in all samples indicate that, despite the coarsening, both Ti and Ag phases remain contiguous, in other words, the bicontinuous structure is preserved even with prolonged annealing time.

### 3.2. Microstructure of partially decomposed samples

A 2 min anneal served to investigate the initial stages of microstructure evolution during reverse peritectic melting. Again, the quenching is fast enough to preserve the partially decomposed structure. Fig. 6(a) shows the microstructure of the partially decomposed sample. Three phases can be found, namely $\alpha$-Ti (dark), TiAg (gray) and Ag (bright). The Ti phase appears granular, as distinguished from the network-like structure of dealloyed porous metals. The Ag phase is located at the grain boundary regions of the original TiAg phase, which is consistent with the foam-like morphology of the Ag phase after longer peritectic melting treatment, Figs. 4 (c, d) above.

Interestingly, the Ti/TiAg interfaces (yellow arrows in Fig. 6) appear predominantly planar. To gain a clearer view of the microstructure, the Ag phase was removed using nitric acid, and the pore space was vacuum-impregnated with epoxy to preserve the structure during the grinding and polishing process. In the resulting SEM micrograph, Fig. 6(b), the epoxy which replaces the Ag phase shows up black. A planar interface is again observed, here connecting TiAg with hemispherical Ti grains. A concave surface can be seen in the TiAg grain opposite the Ti hemisphere, and an interspersed layer of epoxy suggests that the interface on this side of the Ti grains was coated by Ag.

The fracture surface of a partially decomposed sample is shown in Fig. 7, where Ag was again removed by etching. Both TiAg and $\alpha$-Ti are observed, with distinct morphologies. The SEM-EDX data in Table 1 show that the phase with planar surfaces (position 1 and 2 in Fig. 7(b)) is TiAg, while the one with rough surfaces (position 3 and 4 in Fig. 7(b)) is $\alpha$-Ti. The planar surfaces of the TiAg grains confirm the observations from the cross-sections.

A noteworthy feature is the morphology near the triple lines surrounding $\alpha$-Ti/TiAg interfaces in the partially decomposed sample. Arrows in Fig. 7(a) mark this morphology, which is abundant in partially decomposed samples. Fig. 7(b) provides details. Grains of $\alpha$-Ti (for instance at positions 3 and 4) attach to TiAg by a narrow neck that is surrounded by a trench in the TiAg grain, giving the Ti phase a mushroom-like aspect.

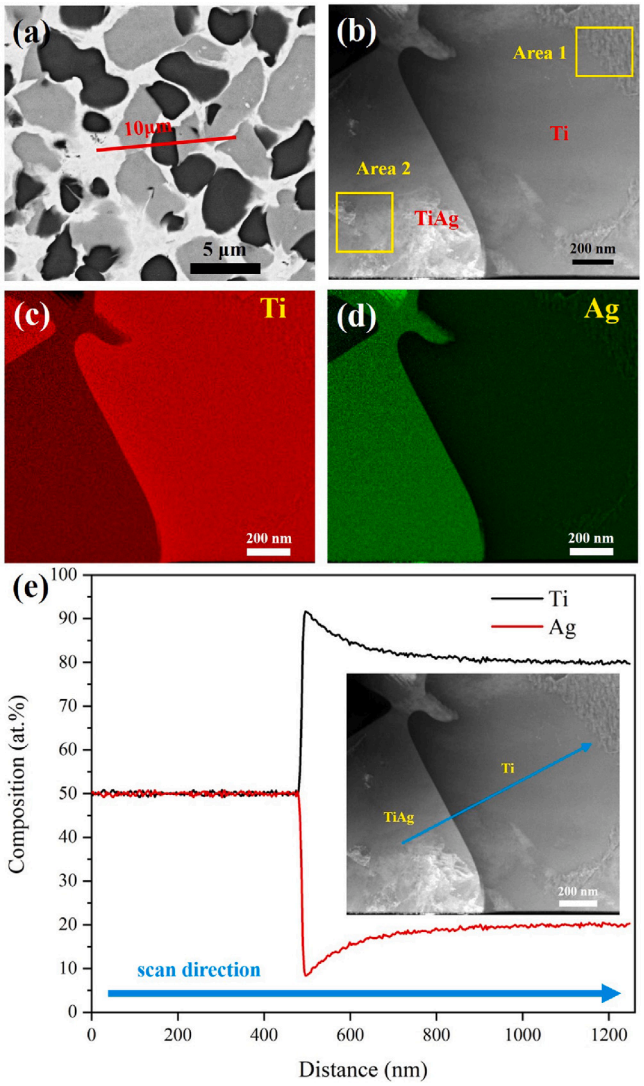


**Fig. 8.** Transmission-electron-microscopy-based composition analysis on a 100 nm thick, focused ion beam (FIB) cut lamella from a partially decomposed sample. (a) Selected area for FIB cutting. (b) High-angle annular dark-field image of the plate; areas selected for quantitative energy-dispersive X-ray (EDX) analysis are indicated by the yellow squares. (c) EDX mapping of Ti. (d) EDX mapping of Ag. (e) EDX line scan across the interface between TiAg and $\alpha$-Ti. No obvious composition change was found in TiAg phase, but composition gradient in $\alpha$-Ti phase was found as the Ag fraction increases in the direction away from the interface. (For interpretation of the references to colour in this figure legend, the reader is referred to the web version of this article.)

**Table 1**
Composition at different positions in partially decomposed sample in Fig. 7(b). Implications for local phase are indicated.

| Position | Ti (at.%) | Ag (at.%) | Phase |
|---|---|---|---|
| 1 | 57.5 | 42.5 | TiAg |
| 2 | 55.2 | 44.8 | TiAg |
| 3 | 84.3 | 15.7 | $\alpha$-Ti |
| 4 | 84.2 | 15.8 | $\alpha$-Ti |

### 3.3. Structure of the Ti/TiAg interface

The Ti/TiAg interface is crucial for the formation mechanism of the Ti phase, which is the microstructure-defining phase in the bicontinuous solid/melt composite formed by the reverse peritectic decomposition of TiAg. For a targeted study of that interface, we have cut a FIB lamella corresponding to the region of the red rectangle in the overview SEM micrograph of Fig. 8(a). This region bisects one of the planar Ti/TiAg interfaces. Fig. 8(b) shows the high-angle annular dark-field image of a region including the interface. Quantitative EDX in areas 1 and 2 suggests Ti (composition: Ti - 80.8 at.%, Ag - 19.2 at.%) on the right of the interface and TiAg (Ti - 50.4 at.%, Ag - 49.6 at.%) on the left. Element mapping for Ti (Fig. 8(c)) and Ag (Fig. 8(d)) confirms that picture.

Ti and Ag line scans perpendicular to the interface are shown in Fig. 8(e). The composition in the TiAg grain is uniform. By contrast, the Ti grain exhibits a composition gradient close to the interface — the Ag fraction increases from about 9 at.% near the interface to a uniform 20 at.% inside the grain.

Bright-field images (Fig. 9(a)) of the FIB lamella show bend contours (suggested by the red arrow). Their undisturbed shape indicates that the Ti phase is a single grain in the vicinity of the interface. Selected area electron diffraction patterns were obtained from Ti and from TiAg regions, as marked by the blue and red circles in Fig. 9(e). The labeled diffraction pattern of the Ti phase (Fig. 9(d)) corresponds to hexagonal closed-pack $\alpha$-Ti ($P6_3/mmc$), with the electron beam oriented along the $[2\bar{1}\bar{1}0]$ zone axis. The diffraction pattern (Fig. 9(f)) reveals the expected body centered tetragonal TiAg (P4/mmm) lattice, with the beam aligned with [111].

Fig. 9(c) shows the diffraction pattern at the interface as a superposition of two sets of spots. Those connected with the yellow rectangle are the diffraction pattern of the $\alpha$-Ti phase, while those connected by the red hexagon represent the pattern of the TiAg phase. Diffraction spots overlap between the (0002) plane of the $\alpha$-Ti and the $(\bar{1}01)$ plane of the TiAg phase, indicating that the two planes are parallel to each other. This relationship is confirmed by the high-resolution TEM image (Fig. 9(b)) of the interface.

While we observe the $\alpha$-Ti/TiAg interface as predominantly planar, Fig. 9 exemplifies that this interface can also exhibit curved segments. A variable orientation of the interface normal is not in contradiction to the well-defined orientation relationship between the underlying crystal lattices, which will now be inspected.

## 4. Discussion

### 4.1. Orientation relationship between the Ti phase and the TiAg phase

The electron diffraction results from Fig. 9 characterize the orientation relationship between two planes of $\alpha$-Ti and TiAg as $(0001)_{\alpha-Ti} \parallel (\bar{1}01)_{TiAg}$. A schematic of their lattice correspondence is illustrated as Fig. 10(a), with the crystallographic data taken from Refs. [39,40]. The (0001) plane of $\alpha$-Ti is shown as the hexagon connected with blue dashed lines, showing six-fold symmetry, while the $(\bar{1}01)$ plane of TiAg is drawn in black, showing a near hexagonal symmetry with small distortion. Due to the difference in lattice symmetry between the two planes, the lattice misfit is compared in two directions. The calculated mismatch at $[010]_{TiAg}$ ($[\bar{1}2\bar{1}0]_{\alpha}$) direction is 1.63%, while at $[111]_{TiAg}$ ($[11\bar{2}0]_{\alpha}$) it is 2.03%. The closeness of fit results in part from the close match of the Ag and Ti atomic radii (148 and 144 pm respectively, calculated from Ref. [40]), and this match also implies that the Ag content of the Ti solid solutions in our alloy will only weakly affect the lattice misfit with TiAg.

Note that $\beta$-Ti, the stable phase at the annealing temperature, transforms to $\alpha$-Ti upon quenching. This prevented a direct investigation of the at-temperature orientation relationship between $\beta$-Ti and TiAg during peritectic melting. Yet, the crystallography after quenching can only be understood if the high-temperature configuration also exhibited a defined orientation relation, and if the transformation to the low-temperature phase was organized so as to maintain crystallographic correlation. In fact, it is known that the $\beta$-to-$\alpha$ transformation in Ti follows the Burgers orientation relationship [45,46], which is characteristic of hcp-bcc transformations (see Fig. 10(b)). Here, $(\bar{1}01)_{\beta-Ti} \parallel (0001)_{\alpha-Ti}$. This would make the observed room-temperature lattice correspondences, namely $(0001)_{\alpha-Ti} \parallel (\bar{1}01)_{TiAg}$, consistent with a lattice

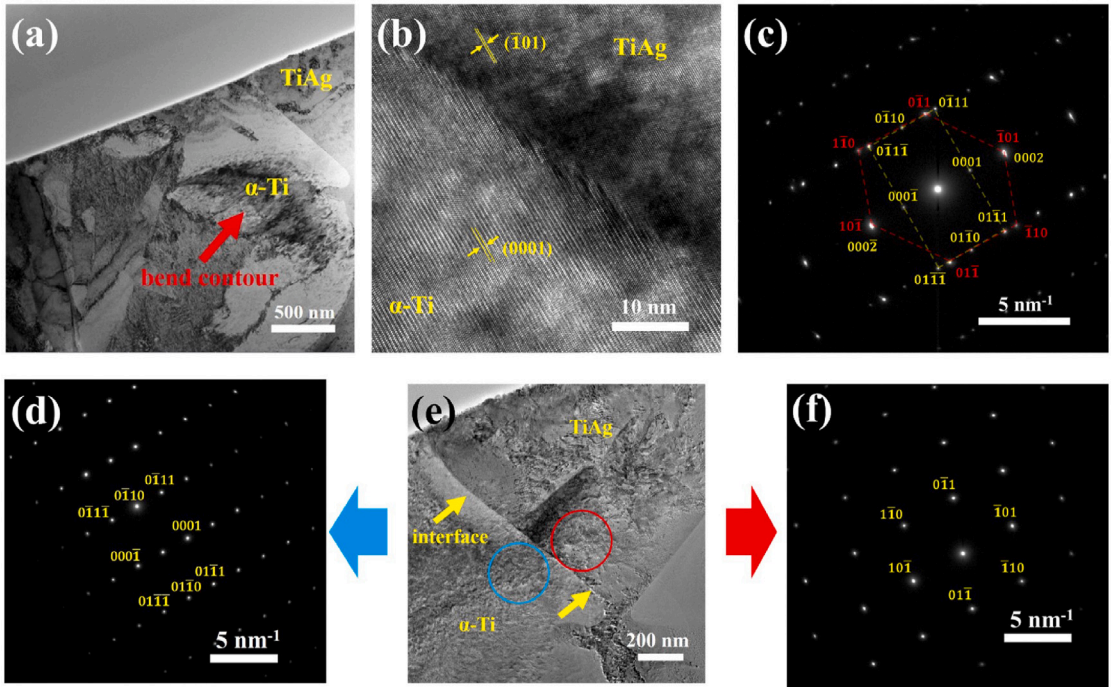


**Fig. 9.** Transmission electron microscopy images and diffraction pattern of focused ion beam cut sample. (a) Bright-field image of the sample plate. No interface was found inside the bend contour, which suggests that the Ti phase is a single grain adjacent to the Ti/TiAg interface. (b) High-resolution image of the interface. (c) Selected area electron diffraction pattern of the interface. Two sets of diffraction pattern can be found, the overlapping spots suggest the orientation relationship between the Ti and the TiAg phase. (d, e, f) Selected area of the sample and the electron diffraction pattern of $\alpha$-Ti phase (d) and TiAg phase (f). (For interpretation of the references to colour in this figure legend, the reader is referred to the web version of this article.)

correspondence at the annealing temperature shown in Fig. 10(c), where $(\bar{1}01)_{\beta-\mathrm{Ti}} \parallel (\bar{1}01)_{\mathrm{TiAg}}$. Our observations on TiAg are then similar to the orientation relationship evolution found during quenching of Ti-Cu alloy [47]. During annealing, $Ti_2Cu$ forms from $\beta$-Ti matrix, following the lattice correspondence $(110)_{\beta-\mathrm{Ti}} \parallel (103)_{\mathrm{Ti_2Cu}}$. In the subsequent quenching process, the orientation relationship in Ti-Cu changed to $(0001)_{\alpha-\mathrm{Ti}} \parallel (103)_{\mathrm{Ti_2Cu}}$, as the phase transformation from $\beta$-Ti to $\alpha$-Ti in that system also follows the Burgers correspondence.

Coherent interfaces with low lattice parameter misfit and large density of coincident sites can have a low specific interfacial excess energy. Thus, the TiAg/Ti interface may act as a favorable heterogeneous nucleation site of Ti. This is consistent with the microstructure of partially decomposed samples, where the newly formed Ti always attach to TiAg grains.

### 4.2. Mechanism of dealloying and its conflict with the present observations

The bicontinuous structure after peritectic melting of TiAg is similar to that produced by LMD, motivating the discussion, in earlier work [13], of peritectic melting as an internal, LMD-like process. However, this notion is not naturally compatible with all observations of the present study. As a background for the discussion, we here introduce the dealloying-like process as it has been previously proposed. Section 4.3 will present an alternative picture that is more readily reconciled with our observations.

Our observations show that the TiAg grain boundaries are wetted by an Ag-rich phase, suggesting grain boundary wetting as the initial stage of peritectic melting. Consumption of the TiAg grains during equilibration could then be considered as an LMD-like process, where the interfaces between grains and wetting films act as dealloying fronts. The schematics of Fig. 11 illustrate this notion. In the hypothetical picture, as dealloying progresses towards the center of the grains, Ag atoms at the wetted surfaces would dissolve into the melt (indicated by red arrows). The resulting enrichment in Ti would tend to passivate the TiAg surface, while lateral diffusion (black arrows) of Ti would mitigate the passivation by relocating this element to newly formed ligaments of the second equilibrium phase, Ti. This mechanism would ensure that the newly formed Ti phase would always remain attached to the master grain, and that the dealloying front would move from grain boundaries into the grain centers.

The above, dealloying-like process is consistent with the bicontinuous microstructure. Yet, it conflicts with several other of the present observations. The notion of a dealloying-like process would require that the Ti–TiAg interface migrates, in crystal coordinates, progressively further into the TiAg grain as that grain is consumed. An atomic-scale mechanism for that migration has not been brought forward. Furthermore, the planarity and coherency of the interfaces in partially decomposed samples are not natural consequences of a dealloying scenario. For areas on the dealloying front that are not covered by Ti, the dealloying process can proceed through surface diffusion. However for areas that are covered with Ti, the Ti and Ag atoms there need to relocate by bulk- or interface diffusion, which should be significantly slower than surface diffusion. The large difference in diffusivity in different areas makes it difficult for the dealloying front to retain a planar interface morphology during peritectic melting.

It is also of interest to inspect composition gradients within the Ti product phase. In a dealloying scenario, the Ti/TiAg interface marks the dealloying front, and Ti regions adjacent to that interface should be the most recently formed Ti. Usually, the newly formed phase exhibits a composition gradient from the dealloying front (recently formed) to the external surface, with the fraction of sacrificial element decreasing in that direction. This has been found in electrochemical dealloying [48], liquid metal dealloying [10] and also vapor phase dealloying [49]. However, our Fig. 8(e) shows the inverse result — the fraction of the sacrificial element (Ag in this study) is depressed right at the interface. It is only around 200 nm away from the interface that the Ag fraction stabilizes at a constant value. The inverse composition gradient is difficult to reconcile with a classic dealloying mechanism.

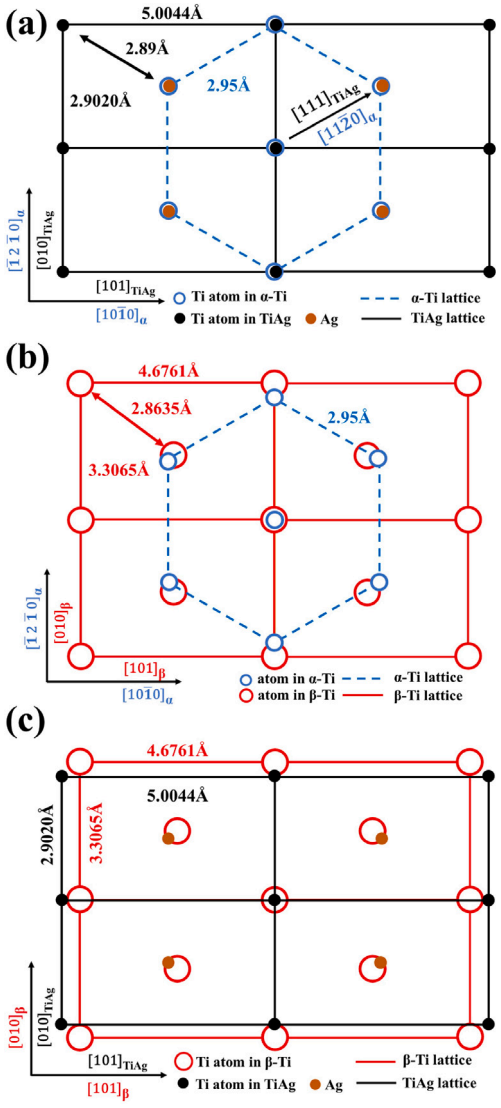


**Fig. 10.** Schematic of orientation relationship between $\alpha$-Ti, $\beta$-Ti and TiAg in a real-space representation. (a) The observed lattice correspondence of $(0001)_{\alpha}$ and $(\bar{1}01)_{TiAg}$ plane. The two lattices have low mismatch. (b) Schematic of Burgers orientation relationship. During quenching, the transformation from $\beta$-Ti to $\alpha$-Ti follows the lattice correspondence $(0001)_{\alpha-Ti} \parallel (\bar{1}01)_{\beta-Ti}$. (c) The possible orientation relationship at annealing temperature between $\beta$-Ti and TiAg as $(\bar{1}01)_{\beta-Ti} \parallel (\bar{1}01)_{TiAg}$. Lattice spacings inferred from crystallographic data in Refs. [39,40].

### 4.3. Microstructure formation by liquid film migration

As an alternative mechanism of bicontinuous microstructure formation during peritectic melting, we now consider liquid film migration, see the schematics in Fig. 12. As we already discussed, peritectic melting starts with grain boundary wetting, panel (a). The observation of wetting suggests grain-boundary premelting. In other words, the melt can nucleate spontaneously, without barrier, at grain boundaries in TiAg. While the equilibrium phase $\beta$-Ti has not yet nucleated, the melt then equilibrates with the pristine TiAg phase. A red dashed line in the alloy phase diagram of Fig. 1(a) schematically illustrates this constrained-equilibrium liquidus line as the extrapolation of the liquidus — representative of the TiAg-melt equilibrium — below the peritectic temperature.

As peritectic melting proceeds, Ti must then nucleate from the supersaturated melt.

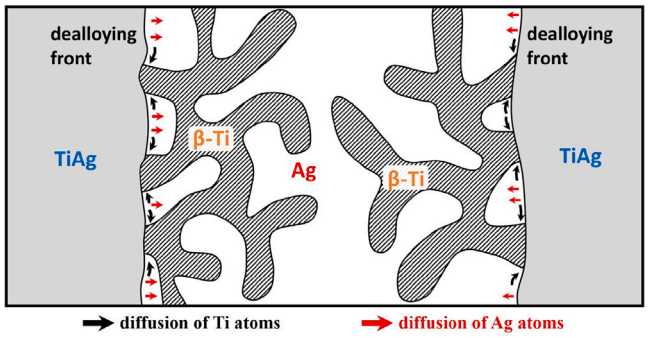


**Fig. 11.** Schematic of the hypothetical dealloying mechanism. $\beta$-Ti forms through surface diffusion of Ti atoms at the dealloying front, as Ag atoms move into the melt. Decomposition started at the wetted grain boundaries, and then go inside the TiAg grain. Note that this mechanism is not compatible with our experimental results, a different mechanism is proposed in this paper. (For interpretation of the references to colour in this figure legend, the reader is referred to the web version of this article.)

The coherent structure of the TiAg/$\beta$-Ti interface and the low lattice mismatch suggest a low interfacial energy, favoring coherent nucleation of $\beta$-Ti at the TiAg surface. This is consistent with the observation on the interface structure. Fig. 12(b) schematically illustrates this stage, and Ti precipitates in an early stage of growth can be observed at the wetted grain boundaries in partially decomposed samples in Fig. 12(d).

In the next stage, the decomposition of TiAg and the growth of $\beta$-Ti continue in a quasi steady-state fashion. Fig. 12(c) schematically illustrates that stage. At receding TiAg surfaces, both Ti and Ag atoms dissolve into the liquid film. Ti and part of the Ag diffuse through the film, normal to the interface, and deposit on its opposite side as Ti. Surplus Ag thickens the film. The continued action of this process forms a concave TiAg surface and a convex $\beta$-Ti one. If the decomposition is interrupted before the base TiAg grain (on the left) has been decomposed by corrosion from other grain boundaries, a hemispherical $\beta$-Ti attached to TiAg by a coherent interface is observed — as in our SEM micrographs (see Fig. 12(e)).

When the decomposition is allowed to proceed to completion, LFM provides a natural pathway for transforming the entire alloy into the new equilibrium phases. Upon quenching, $\beta$-Ti will transform to $\alpha$-Ti while the interface remains coherent, as discussed in Section 3.3.

As a side effect of the above process, the TiAg/Ti interfaces are bounded by a TiAg/Ti/liquid Ag triple lines. Those lines may provide for a different, local decomposition mode, which has been the subject of earlier numerical study [36,50]. A schematic is shown as Fig. 13(a). Here, the triple point recedes while the Ti/TiAg interface is attacked. Jointly, dissolution from TiAg and deposition on Ti create two parabolic surfaces. The result is a mushroom-like morphology of the residual TiAg. This mushroom-like structure can be seen in the micrographs of Figs. 13(b) and 7(b).

Why will the processes discussed so far result in a bicontinuous microstructure rather than disconnected Ti grains wetted by the melt? That question has been discussed, in an analogous scenario, for partial melting of Cu–In [15]. The reference points towards partial wetting scenarios, in which a fraction of the boundaries remain connected, not completely wetted. The microstructure can then exhibit contiguous solid pathways that form the continuous skeleton of one of the two bicontinuous phases. In fact, Fig. 3 shows evidence for partial wetting in partially molten TiAg, suggesting that the present alloy exhibits the same mechanism as Cu–In.

The suggested mechanism of the reverse peritectic transformation is naturally consistent with our observation of composition gradients at the Ti/TiAg interface. It is well understood that precipitation from a supersaturated solution leads to a composition change in the precipitate. The parallel tangent construction [51–53] in the schematic molar Gibbs energy diagram of Fig. 14 provides an illustration. The

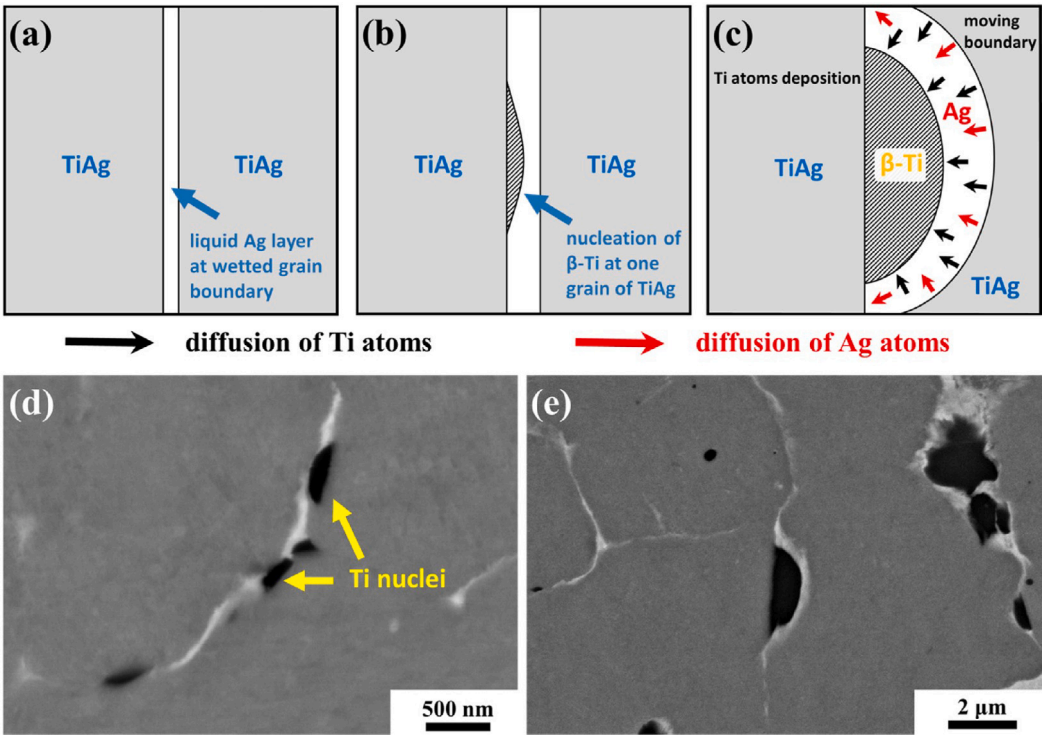


**Fig. 12.** Microstructure evolution during peritectic melting through LFM mechanism. (a) Grain boundary of TiAg wetted by liquid Ag at the beginning of peritectic melting. (b) Nucleation of $\beta$-Ti at the TiAg/liquid melt interface (c) Decomposition of one TiAg grain. Both Ti and Ag atoms dissolve into the melt, and Ti atoms redeposit on the already nucleated $\beta$-Ti. (d) Backscattered electron (BSE) image of a partially decomposed sample, multiple Ti nuclei can be found at the wetted surface. (e) BSE image showing the correspondence intermediate structure illustrated in (c).

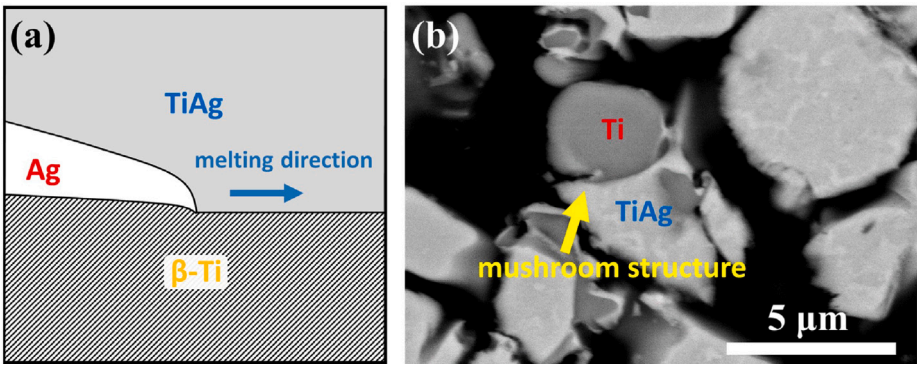


**Fig. 13.** Schematic of melting along TiAg/Ti interface. (a) Dissolution of TiAg and deposition of Ti along the Ti/TiAg interface. (b) The mushroom-like structure found in a partially decomposed sample, as a corresponding structure in (a).

figure refers to annealing above the equilibrium peritectic temperature. The stable phases are then $\beta$-Ti and the melt, and their composition at equilibrium (once the transformation is complete) is identified by the common tangent to their free energy functions. Yet, at the onset of the transformation, TiAg represents the majority phase. Initially, TiAg coexists with the melt, as that phase can nucleate without barrier at wetted grain boundaries or triple junctions in TiAg. The TiAg/Ag common tangent determines the equilibrium compositions constrained by the absence of the stable $\beta$-Ti phase. Inspection of Fig. 14 reveals that the melt is then initially depleted in silver, as compared to the Ti/Ag equilibrium. When the $\beta$-Ti solid solution precipitates from the melt, the secondary (parallel) tangent identifies the composition of maximum driving force. This again corresponds to a silver-depleted solution. As the reverse peritectic transformation proceeds, the TiAg phase gradually vanishes and the Ti/Ag equilibrium approaches the condition described by the equilibrium common tangent. The composition gradients in the Ti phase near its interface with TiAg document the transition from silver-depleted solution at the onset of Ti precipitation to equilibrated solution in the later growth stages.

An essential characteristic of the LFM process of microstructure formation during the reverse peritectic transformation is the dissolution and then redeposition of the majority component of the new solid phase, here Ti. The dissolution/redeposition mechanism is considered insignificant for aqueous dealloying of noble metal alloys, because of the low solubility of the more-noble component in the liquid [54]. By contrast, the mechanism may be generic to LMD, where the network-forming component typically has a finite solubility in the melt. Even then, LFM is distinguished from LMD by the direction of the diffusion fluxes relative to the interface. Whereas LMD requires normal transport of the sacrificial component through the melt and lateral transport of the solid, network-forming component [55,56], LFM requires the opposite, namely normal transport of the network former and, ultimately, lateral transport (out of the boundary region) of the major molten component.

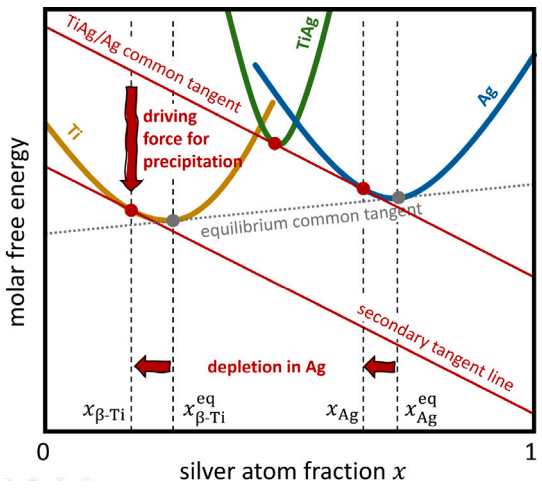


**Fig. 14.** Schematic molar free energy diagram explaining the silver depletion in $\beta$-Ti at the onset of Ti precipitation early-on during the reverse peritectic transformation. Colored curved graphs: free energies of the phases at the annealing temperature, slightly above the equilibrium peritectic temperature. Equilibrium phases are $\beta$-Ti ("Ti", yellow line) and silver-rich melt ("Ag", blue line); their silver atom fractions, $x^{eq}_{\beta-Ti}$ and $x^{eq}_{Ag}$ at equilibrium are determined by the equilibrium common tangent (dashed gray line). Before the onset of Ti precipitation, the melt is at equilibrium with the TiAg parent phase ("TiAg", green line); the TiAg/Ag common tangent implies silver depletion in the melt, $x_{Ag} < x^{eq}_{Ag}$. With Ti precipitating from the melt, the secondary tangent line determines that silver fraction, in the precipitate, at which the driving force for precipitation is at maximum. This again implies silver depletion, here in $\beta$-Ti, $x_{\beta-Ti} < x^{eq}_{\beta-Ti}$. (For interpretation of the references to colour in this figure legend, the reader is referred to the web version of this article.)

## 5. Conclusions

Starting out from the earlier report promoting peritectic melting in TiAg as producing bicontinuous microstructure by a through-bulk dealloying process, our study explores the underlying microstructure evolution. We reproduce the bicontinuity of both product phases, Ti and Ag and the scheme for producing either one of the phases as a porous solid by removing the respective of the phase. Yet, our observations do not characterize the underlying mechanism as dealloying.

Whereas dealloying is characterized by a competition between corrosion and passivation and by lateral transport of the constituents of the solid product phase along the corrosion front, our observations suggest that the product phase grows by normal transport across liquid films that originally wet the grain boundaries of the master alloy. The films then equilibrate the system by sweeping the master alloy grains. As support of that notion we advertise the well-defined orientation relationship and the composition gradients at interfaces between product and master alloy phase in the partially decomposed alloy. A local dissolution/redeposition process at TiAg/Ti/melt triple lines is consistent with that picture.

This work offers a new explanation of the peritectic melting process of TiAg and of the associated formation of a bicontinuous microstructure. By clarifying the underlying microstructure evolution process, the findings may provide a basis for identifying other alloy systems with peritectic transformations that may also be suitable for producing bicontinuous or porous microstructures in a through-bulk, scalable process.

## CRediT authorship contribution statement

**Zhongyang Li:** Writing – original draft, Methodology, Investigation, Conceptualization. **Lukas Lührs:** Writing – review & editing, Supervision, Conceptualization. **Tobias Krekeler:** Investigation. **Jörg Weissmüller:** Writing – review & editing, Supervision, Funding acquisition, Conceptualization.

## Acknowledgments

This work was supported by the Deutsche Forschungsgemeinschaft (DFG), Germany within the Collaborative Research Centre CRC 986 "Tailor-Made Multi-Scale Materials Systems" (Project No. 192346071) and by the China Scholarship Council, China.

## References

[1] I. McCue, E. Benn, B. Gaskey, J. Erlebacher, Dealloying and dealloyed materials, Annu. Rev. Mater. Res. 46 (2016) 263–286.
[2] H.-J. Jin, J. Weissmüller, A material with electrically tunable strength and flow stress, Science 332 (2011) 1179–1182.
[3] Y. An, Y. Tian, C. Wei, Y. Tao, B. Xi, S. Xiong, J. Feng, Y. Qian, Dealloying: An effective method for scalable fabrication of 0D, 1D, 2D, 3D materials and its application in energy storage, Nano Today 37 (2021) 101094.
[4] Z. Zhang, Y. Wang, Z. Qi, W. Zhang, J. Qin, J. Frenzel, Generalized fabrication of nanoporous metals (Au, Pd, Pt, Ag, and Cu) through chemical dealloying, J. Phys. Chem. C 113 (2009) 12629–12636.
[5] Z. Qi, C. Zhao, X. Wang, J. Lin, W. Shao, Z. Zhang, X. Bian, Formation and characterization of monolithic nanoporous copper by chemical dealloying of Al–Cu alloys, J. Phys. Chem. C 113 (2009) 6694–6698.
[6] L. Lührs, J. Weissmüller, Nanoporous copper-nickel–macroscopic bodies of a strong and deformable nanoporous base metal by dealloying, Scr. Mater. 155 (2018) 119–123.
[7] K. Sieradzki, N. Dimitrov, C. McCall, N. Vasiljevic, J. Erlebacher, The dealloying critical potential, J. Electrochem. Soc. 149 (2002) B370.
[8] T. Wada, K. Yubuta, A. Inoue, H. Kato, Dealloying by metallic melt, Mater. Lett. 65 (2011) 1076–1078.
[9] Z. Lu, C. Li, J. Han, F. Zhang, P. Liu, H. Wang, Z. Wang, C. Cheng, L. Chen, A. Hirata, et al., Three-dimensional bicontinuous nanoporous materials by vapor phase dealloying, Nat. Commun. 9 (2018) 276.
[10] I. McCue, B. Gaskey, P.-A. Geslin, A. Karma, J. Erlebacher, Kinetics and morphological evolution of liquid metal dealloying, Acta Mater. 115 (2016) 10–23.
[11] L. Huang, M. Liu, H. Lin, Y. Xu, J. Wu, V.P. Dravid, C. Wolverton, C.A. Mirkin, Shape regulation of high-index facet nanoparticles by dealloying, Science 365 (2019) 1159–1163.
[12] J. Erlebacher, M.J. Aziz, A. Karma, N. Dimitrov, K. Sieradzki, Evolution of nanoporosity in dealloying, Nature 410 (2001) 450–453.
[13] W.-K. Hu, J.-C. Shao, S.-G. Wang, H.-J. Jin, Evolution of a bicontinuous structure in peritectic melting: The simplest form of dealloying, Phys. Rev. Mater. 3 (2019) 113601.
[14] O. Dezellus, R. Arroyave, S.G. Fries, Thermodynamic modelling of the Ag–Cu–Ti ternary system, Int. J. Mater. Res. 102 (2011) 286–297.
[15] Z. Li, L. Lührs, J. Weissmüller, Bicontinuous microstructure formation through partial melting, Scr. Mater. 250 (2024) 116192.
[16] B. Young-Joon, D.N. Yoon, Migration of liquid film and grain boundary in mo-ni induced by temperature change, Acta Metall. 33 (1985) 1911–1917.
[17] J.Y. Ko, S.-Y. Park, D.Y. Yoon, S.-J.L. Kang, Migration of intergranular liquid films and formation of core–shell grains in sintered TiC–Ni bonded to Wc–Ni, J. Am. Ceram. Soc. 87 (2004) 2262–2267.
[18] A. King, Diffusion induced grain boundary migration, Int. Mater. Rev. 32 (1987) 173–189.
[19] I. Manna, S. Pabi, W. Gust, Discontinuous reactions in solids, Int. Mater. Rev. 46 (2001) 53–91.
[20] D.N. Yoon, W.J. Huppmann, Chemically driven growth of tungsten grains during sintering in liquid nickel, Acta Metall. 27 (1979) 973–977.
[21] W. McPhee, G. Schaffer, J. Drennan, The effect of iron on liquid film migration and sintering of an Al–Cu–Mg alloy, Acta Mater. 51 (2003) 3701–3712.
[22] R.A. Woods, Liquid Film Migration During Aluminum Brazing, Technical Report, SAE Technical Paper, 1997.
[23] M. Benoit, M. Whitney, M. Wells, H. Jin, S. Winkler, Liquid film migration in warm formed aluminum brazing sheet, Metall. Mater. Trans. A 48 (2017) 4645–4654.
[24] A. Wittebrood, C. Kooij, K. Vieregge, Grain boundary melting or liquid film migration in brazing sheet, in: Mater. Sci. Forum, vol. 331, Trans Tech Publ, 2000, pp. 1743–1750.
[25] O. Ojo, N. Richards, M. Chaturvedi, Liquid film migration of constitutionally liquated $\gamma'$ in weld heat affected zone (HAZ) of inconel 738lc superalloy, Scr. Mater. 51 (2004) 141–146.
[26] B. Radhakrishnan, R. Thompson, Liquid film migration (LFM) in the weld heat affected zone (HAZ) of a Ni-base superalloy, Scr. Metall. Mater. 24 (1990) 537–542.
[27] P. Peng, Migration of liquid particle from mushy zone interface in temperature gradient, Int. J. Heat Mass Transfer 142 (2019) 118467.
[28] P. Peng, X. Li, J. Li, Y. Su, J. Guo, H. Fu, On migration of primary/peritectic interface during interrupted directional solidification of Sn–Ni peritectic alloy, Sci. Rep. 6 (2016) 24512.

[29] J.K. Kim, D.Y. Yoon, The suppression of chemically induced liquid film migration in Co–Cu at high temperature, Acta Metall. Mater. 42 (1994) 913–919.
[30] T. Muschik, W. Kaysser, T. Hehenkamp, Melting of Cu–In solid solutions at small superheating by droplet formation and liquid film migration, Acta Metall. 37 (1989) 603–613.
[31] E. Rabkin, B. Straumal, L. Shvindlerman, R. Fournelle, W. Gust, High temperature digm in an Fe–5 At.% Al bicrystal during zinc diffusion, Scr. Metall. Mater. 26 (1992) 901–906.
[32] R. Chaim, A.H. Heuer, D.G. Brandon, Phase equilibration in $ZrO_2$-$Y_2O_3$ alloys by liquid-film migration, J. Am. Ceram. Soc. 69 (1986) 243–248.
[33] H.K. Schmid, Diffusion-induced grain-boundary migration in ceria-stabilized tetragonal zirconia polycrystals, J. Am. Ceram. Soc. 74 (1991) 387–394.
[34] K.-W. Chae, D.-I. Chun, D.-Y. Kim, Y.-J. Baik, K.-Y. Eun, Microstructural evolution during the infiltration treatment of titanium carbide-iron composite, J. Am. Ceram. Soc. 73 (1990) 1979–1982.
[35] Y.-J. Baik, K.Y. Eun, Chemically induced migration of liquid films and grain boundaries in TiN—Ni—(TiC) alloy, J. Am. Ceram. Soc. 74 (1991) 1397–1400.
[36] G. Boussinot, E. Brener, D. Temkin, Kinetics of isothermal phase transformations above and below the peritectic temperature: Phase-field simulations, Acta Mater. 58 (2010) 1750–1760.
[37] A. Viardin, G. Boussinot, J. Zollinger, Phase field modeling of partial remelting during reheating of a multiphase peritectic solidification microstructure, Materialia 26 (2022) 101590.
[38] N. Reilly, B. Rouat, G. Martin, D. Daloz, J. Zollinger, Enhanced dendrite fragmentation through the peritectic reaction in tial-based alloys, Intermetallics 86 (2017) 126–133.
[39] R. Van Thyne, W. Rostoker, H. Kessler, Observations on the phase tiag, Trans. Am. Inst. Min. Met. Pet. Eng. 197 (1953) 670–671.
[40] R.W.G. Wyckoff, R.W. Wyckoff, Crystal Structures, vol. 1, Interscience publishers, New York, 1963.
[41] ICDD, PDF-2 Database Sets 1-45 Plus 70-86, The International Centre for Diffraction Data Newtown Square, PA, USA, 1999.
[42] H.E. Swanson, Standard X-Ray Diffraction Powder Patterns, vol. 25, US Department of Commerce, National Bureau of Standards, 1953.
[43] R. Sailer, G. McCarthy, ICDD Grant-in-Aid, North Dakota State university, Fargo, North Dakota, USA, 1993.
[44] W.-K. Hu, L.-Z. Liu, L. Zou, J.-C. Shao, S.-G. Wang, H.-J. Jin, Synthesis and mechanical properties of porous metals with inverted dealloying structure, Scr. Mater. 210 (2022) 114483.
[45] W. Burgers, On the process of transition of the cubic-body-centered modification into the hexagonal-close-packed modification of zirconium, Physica 1 (1934) 561–586.
[46] T. Furuhara, S. Takagi, H. Watanabe, T. Maki, Crystallography of grain boundary $\alpha$ precipitates in a $\beta$ titanium alloy, Metall. Mater. Trans. A 27 (1996) 1635–1646.
[47] H. Donthula, B. Vishwanadh, T. Alam, T. Borkar, R. Contieri, R. Caram, R. Banerjee, R. Tewari, G. Dey, S. Banerjee, Morphological evolution of transformation products and eutectoid transformation (s) in a hyper-eutectoid Ti-12 At.% Cu alloy, Acta Mater. 168 (2019) 63–75.
[48] C. Mahr, J.A. Tapia Burgos, M. Schowalter, A. Wittstock, A. Rosenauer, Investigation of the dealloying front in partially corroded alloys, Mater. Res. Lett. 10 (2022) 824–831.
[49] Y. Xia, Z. Lu, J. Han, F. Zhang, D. Wei, K. Watanabe, M. Chen, Bulk diffusion regulated nanopore formation during vapor phase dealloying of a Zn–Cu alloy, Acta Mater. 238 (2022) 118210.
[50] E.A. Brener, D. Temkin, Melting of alloys along the inter-phase boundaries in eutectic and peritectic systems, Acta Mater. 55 (2007) 2785–2789.
[51] J.C. Baker, J.W. Cahn, Thermodynamics of Solidification, American Society for Metals, Metals Park, Ohio, 1971, pp. 23–58.
[52] M. Hillert, Phase Equilibria, Phase Diagrams and Phase Transformations: Their Thermodynamic Basis, second ed., Cambridge University Press, Cambridge, UK, 2008.
[53] K.G.F. Janssens, D. Raabe, E. Kozeschnik, M.A. Miodownik, B. Nestler, Computational Materials Engineering: An Introduction to Microstructure Evolution, Academic Press, 2010.
[54] Q. Chen, K. Sieradzki, Mechanisms and morphology evolution in dealloying, J. Electrochem. Soc. 160 (2013) C226–C231.
[55] P.A. Geslin, I. McCue, B. Gaskey, J. Erlebacher, A. Karma, Topology-generating interfacial pattern formation during liquid metal dealloying, Nature Commun. 6 (2015) 8887.
[56] L. Lesage, T. Suga, T. Wada, H. Kato, C. Le Bourlot, E. Maire, N. Mary, P.-A. Geslin, A diffusion model for liquid metal dealloying. Application to nicu precursors dealloyed in liquid Ag, Acta Mater. 272 (2024) 119908.